Optimal Temperature Estimation for Modeling the Thermal Elastic Shock Disturbance Torque

Darrell F. Zimbelman* and Raymond V. Welch†
Fairchild Space & Defense Corporation, Germantown, Maryland 20879
and
George H. Born‡
University of Colorado, Boulder, Colorado 80309

This paper describes a predictive temperature estimation technique that can be used to drive a model of the thermal elastic shock disturbance torque experienced by low-Earth-orbiting spacecraft. The twice per orbit impulsive disturbance torque is attributed to vehicle passage in and out of the Earth's umbra, during which large flexible appendages undergo rapidly changing thermal conditions. Flexible members, in particular, solar arrays, experience rapid cooling during umbra entrance and rapid heating during exit. The fundamental equations used to model the thermal elastic shock disturbance torque for a typical solar array will be described. For this derivation, the array is assumed to be a thin cantilevered beam. The time-varying thermal gradient is shown to be the driving force behind predicting the thermal elastic shock disturbance torque and, therefore, motivates the need for accurate estimates of temperature. Thus, the development of a technique to optimally estimate appendage surface temperatures is highlighted. The objective analysis method used is structured on the Gauss-Markov theorem and provides an optimal temperature estimate at a prescribed location given data from a distributed thermal sensor network. The optimally estimated surface temperatures are then used to compute the thermal gradient across the array.

Nomenclature

A_{jk} = covariance between all pairs of observations
a = inertial displacement constant
b = temperature bias for gradient function
C_e = error matrix associated with the estimate
C_x = $n_1 \times n_1$ moment matrix of the estimate, $E(xx^T)$
C_{xj} = covariance between the estimate and the jth observation
$C_{x\boldsymbol{\Theta}}$ = $n_1 \times n_2$ moment matrix of the estimate and the observations, $E(x\boldsymbol{\Theta}^T)$
$C_{\boldsymbol{\Theta}}$ = $n_2 \times n_2$ moment matrix of the observations, $E(\boldsymbol{\Theta}\boldsymbol{\Theta}^T)$
c = temperature scaling for gradient function
d = thickness of a typical solar array
E = expected value operator
$f(t-\tau)$ = array inertial displacement function
H_b = thermal elastic shock disturbance momentum
I = inertia about fixed end of structure
I_b = inertial displacement of structure
L = array length
l_i = ith inertia length increment
M = array mass
m_i = ith mass increment
N = total number of observations
n = total number of array segments
p = decay constant for gradient function
q = temperature constant for gradient function
$\bar{r}_{jk}$ = scaling parameter between the jth and kth observations in the r direction
r_{scale} = spatial decorrelation scale in the r direction
s_i = arc length the ith mass increment travels
$\bar{s}_{jk}$ = scaling parameter between the jth and kth observations in the s direction
s_{scale} = spatial decorrelation scale in the s direction
T_b = thermal elastic shock disturbance torque
T_ζ = impulsive portion of thermal elastic shock disturbance torque
$u(t-\tau)$ = unit step function
$\dot{u}(t-\tau)$ = Dirac function
$\ddot{u}(t-\tau)$ = doublet function
W_{jk} = weighting function
x = $n_1 \times 1$ state vector
$\hat{x}$ = $n_1 \times 1$ estimate vector
α_{cte} = coefficient of thermal expansion
γ = measurement degradation factor
ΔT = thermal gradient across the solar array
δ_{jk} = Kronecker delta function
ϵ_j = jth measurement error
$\bar{\boldsymbol{\Theta}}$ = estimated mean of the observations
$\hat{\boldsymbol{\Theta}}$ = optimal estimate
$\Theta(r,s)$ = scalar variable at position (r,s)
θ_i = angle through which the ith mass increment travels
λ = ratio of inertia length increment and radius of curvature
ρ_b = radius of curvature
σ_φ = standard deviation of the observations
σ_ϵ = standard deviation of the measurement error
τ = time of shadow entrance or exit
φ_j = jth measurement
$\bar{\varphi}$ = mean of the observations
i = ith array segment

Introduction

IN the early 1980s, an unexpected perturbation was experienced by the LANDSAT 4 and 5 satellites. An anomously large, twice per orbit disturbance was observed in the flight data during normal on-orbit operations. An example of this disturbance is illustrated in Fig. 1, which shows the LANDSAT-4 yaw axis derived rate telemetry data over one orbital period.[1] These data represent the controlled response of the

---

Received Nov. 14, 1990; revision received April 1, 1991; accepted for publication April 2, 1991.

*Senior Engineer, Guidance, Navigation, and Control Department, M/S G-43. Member AIAA.

†Senior Director, Guidance, Navigation, and Control Department, M/S G-43. Member AIAA.

‡Director, Colorado Center for Astrodynamics Research, Campus Box 431. Fellow AIAA.

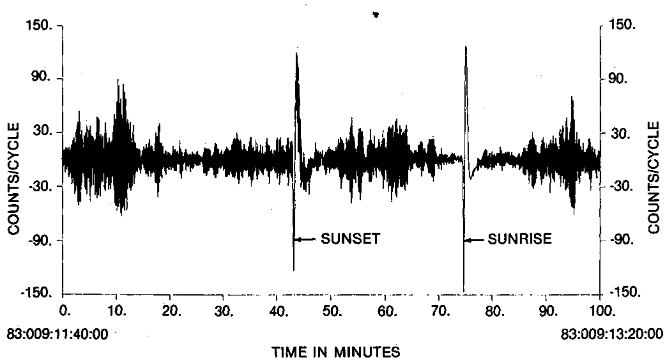

*Where: 1 count = 0.05 Arcseconds and 1 cycle = 0.512 Seconds

Fig. 1 LANDSAT-4 yaw axis derived rate telemetry data over one orbit.

spacecraft coupled with the disturbances acting on the vehicle. The perturbation shown in Fig. 1 has been correlated with the spacecraft's entrance (sunset) and exit (sunrise) to the eclipsed region of the orbit plane.[2] During penumbral transitions, space vehicles undergo rapidly changing thermal conditions that result in a thermally induced bending motion of large flexible appendages. If the deformation or bending motion occurs at a nonconstant rate, a disturbance torque is generated about the fixed end of the structure, which is then transferred back onto the vehicle core body. This concept is illustrated in Fig. 2. For the LANDSAT satellites, the single, large solar array experienced this phenomena and produced the disturbance torque that is evident in Fig. 1.

The aforementioned thermally induced disturbance, referred to as thermal elastic shock (TES), has also been observed during the three-axis stabilized operation of the Communications Technology Satellite (CTS)[3] and normal on-orbit operation of the Hubble Space Telescope (HST),[4] but to a much lesser degree. The difference in perturbation magnitude is a result of the differences between the spacecraft designs. The TES disturbance is most pronounced for asymmetric satellite configurations, such as the single-wing LANDSAT vehicles. Satellites possessing a dual-wing array design, such as CTS and HST, are significantly less affected by TES since the motion of both arrays tends to be self-compensating.

The significant attitude excursions experienced by the LANDSAT vehicles in response to the TES disturbance have aroused considerable concern for future satellite missions. This concern is especially true for the Upper Atmospheric Research Satellite (UARS) and the Topography Experiment (TOPEX) satellite since both vehicles utilize LANDSAT heritage. In particular, the TES disturbance has been predicted to be a dominant source of attitude error for the TOPEX spacecraft.[5] The attitude pointing performance of the TOPEX spacecraft, when subjected to the TES disturbance, has been analyzed by Zimbelman.[6] This study concluded that the TES disturbance is large enough to cause the TOPEX spacecraft to temporarily exceed its normal mission mode attitude control pointing requirements. Thus, for TOPEX and other future satellites, a need is established to accurately model the on-orbit magnitude of the TES disturbance in order to compensate science data taken during degraded attitude periods.

The focus of this paper is to present the fundamental equations used to model the TES disturbance experienced by some Earth orbiting spacecraft. During the development of the equations, the thermal gradient is shown to be the driving force behind predicting the TES disturbance torque. The dependance of the TES model on the thermal gradient motivates the need for accurate estimates of surface temperatures during on-orbit operations. Next, a technique to optimally estimate appendage surface temperatures at prescribed locations given data from a distributed thermal sensor network is highlighted. The objective analysis method, structured on the Gauss-Markov theorem, is described in detail. This technique is advantageous since it provides not only an estimate of the surface temperatures, but also error information relative to the estimates. Examples illustrating the use of the optimal estimation routine to compute the thermal gradient across a typical satellite solar array are given.

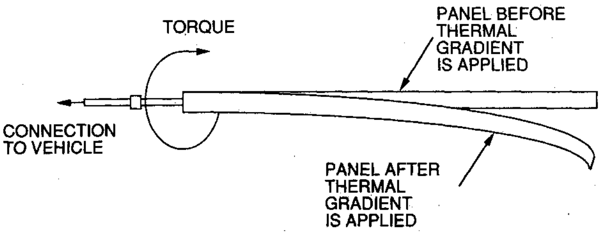

Fig. 2 Appendage structural deflection due to an applied thermal gradient.

Thermal Elastic Shock Disturbance Model

A mathematical representation for the TES disturbance torque for a typical satellite solar array has been developed by Zimbelman.[6] The TES disturbance model uses the concept of linear thermal expansion to describe the angle through which a structure will bend under the influence of thermal heating. Utilizing this physical principle, the radius of curvature can be expressed as

$$\rho_b = \frac{d}{\alpha_{\mathrm{cte}}\Delta T} \tag{1}$$

Equation (1) holds true for both the top and bottom surfaces of the structure under the assumption that the separation distance is small. Now assume that the structure can be represented as a thin cantilevered beam of length L and mass M. A discrete representation for the inertia about the fixed end of the beam is given by

$$I = \sum_{i=1}^{n}\left\{\frac{1}{12}\left(\frac{L}{n}\right)^2 m_i + \left[\frac{L}{n}\left(i-\frac{1}{2}\right)\right]^2 m_i\right\} \tag{2}$$

where the ith mass element is expressed as

$$m_i = M/n \tag{3}$$

Factoring out the mass term, Eq. (2) can be rewritten as an equivalent inertia distribution (lumped mass) given as

$$I = \sum_{i=1}^{n} l_i^2 m_i \tag{4}$$

where l_i is of the form

$$l_i = \sqrt{\frac{1}{12}\left(\frac{L}{n}\right)^2 + \left[\frac{L}{n}\left(i-\frac{1}{2}\right)\right]^2} \tag{5}$$

Next, let I_b be an equivalent inertial displacement defined as the beam inertia multiplied by the angle through which the structure rotates relative to the constrained end

$$I_b = \sum_{i=1}^{n} l_i^2 m_i \theta_i \tag{6}$$

The beam is assumed to deform in a circular arc of radius ρ_b under the influence of a uniform temperature gradient applied over the entire length. The arc length that each element of mass travels is given by

$$s_i = l_i \theta_i \tag{7}$$

The change in radius of curvature associated with each l_i is expressed as

$$\Delta\rho_b = \rho_b - \rho_b\cos(\phi_i) \tag{8}$$

where the curvature angle ϕ_i is given by

$$\tan\phi_i = l_i/\rho_b \tag{9}$$

If the assumption is made that each inertia length increment is small compared to the radius of curvature, such that the ratio $l_i/\rho_b < 0.176$, then the curvature angle $\phi_i < 10$ deg. Under this approximation, the curvature angle for the ith element reduces to

$$\phi_i \approx l_i/\rho_b \tag{10}$$

Physically, this assumption imposes a stiffness constraint on the structure. Assuming the beam to be fairly rigid, each mass element will only travel through a small angle, i.e., $\theta_i < 10$ deg, such that the arc length s_i is approximately linear and equal to the change in radius of curvature given by Eq. (8). Substituting Eqs. (7), (8), and (10) into the derived expression for I_b, Eq. (6), yields

$$I_b \approx \sum_{i=1}^{n} l_i m_i \rho_b \left[1 - \cos\left(\frac{l_i}{\rho_b}\right)\right] \tag{11}$$

The development of the TES disturbance model through Eq. (11) is consistent with the derivation given by Jasper and Neste.[2] Equation (11) defines a general analytical expression to describe the dynamic motion of a thin cantilevered beam of finite thickness given an applied thermal gradient. This equation can also be used to represent the movement of thin flat plates since both geometric figures share a common expression for the inertia about one end.

Intuitively, the first and second time derivatives of Eq. (11) will yield the momentum and torque time histories describing the TES disturbance. An inspection of the LANDSAT-4 derived rate telemetry data (Fig. 1) reveals that the controlled response of the vehicle exhibits an impulsive velocity in one direction immediately followed by a similar motion in the opposite direction and, finally, a decaying step of the initial sign. This responsive rate motion indicates that the angular attitude deviation of the vehicle is represented as an impulsive error in one direction followed by an exponentially decaying step error of opposite sign. Since the LANDSAT satellite attitude control system was designed to exhibit good command following performance, it is assumed that the TES disturbance torque possesses the same two-phase function characteristic, i.e., an impulse followed by an exponentially decaying step of opposite sign. However, the resulting torque function calculated using Eq. (11) only captures the latter part (i.e., the exponentially decaying step) of the overall disturbance. This is because I_b is a multivalued function at $t = \tau$, which yields a step discontinuity at $t = \tau$ for the first time derivative of I_b. Neglecting the step discontinuity in the second time derivative eliminates the impulsive term present in the expected structure of the disturbance torque. Thus, in order to capture the disturbance torque function that completely characterizes the observed on-orbit attitude response, fundamental continuous theoretical functions are derived to explain the underlying mathematics behind the TES phenomena. In the following development, a continuous function for I_b, analogous to the discrete I_b expression given in Eq. (11), will be developed.

Define I_b as a continuous function of the form

$$I_b = a[u(t + \infty) - u(t - \tau)] + f(t - \tau)u(t - \tau) \tag{12}$$

where $u(t - \tau)$ is a unit step function defined as

$$\begin{aligned} u(t - \tau) &= 0 \qquad \text{if} \quad t < \tau \\ &= 1 \qquad \text{if} \quad t \geq \tau \end{aligned} \tag{13}$$

For I_b to be continuous at $t = \tau$, the following matching condition must hold true:

$$f(t - \tau)|_{t=\tau} = a \tag{14}$$

Computing the first and second time derivatives of Eq. (12), and at the same time neglecting all terms involving derivatives of the unit step function $u(t + \infty)$, gives the following expressions for the momentum and torque, respectively,

$$H_b = -a\dot{u}(t - \tau) + f(t - \tau)\dot{u}(t - \tau) + \dot{f}(t - \tau)u(t - \tau) \tag{15}$$

$$\begin{aligned} T_b = {} & -a\ddot{u}(t - \tau) + f(t - \tau)\ddot{u}(t - \tau) \\ & + 2\dot{f}(t - \tau)\dot{u}(t - \tau) + \ddot{f}(t - \tau)u(t - \tau) \end{aligned} \tag{16}$$

where $\dot{u}(t - \tau)$ is a Dirac function described as

$$\begin{aligned} \dot{u}(t - \tau) &= \infty \qquad \text{if} \quad t = \tau \\ &= 0 \qquad \text{otherwise} \end{aligned} \tag{17}$$

The doublet $\ddot{u}(t - \tau)$ in Eq. (16) that is multiplied by the function $f(t - \tau)$ can be expressed as two terms[7]

$$f(t - \tau)\ddot{u}(t - \tau) = f(0)\ddot{u}(t - \tau) - \dot{f}(0)\dot{u}(t - \tau) \tag{18}$$

Finally, if the matching condition, Eq. (14), and the doublet equation, Eq. (18), are applied to both Eqs. (15) and (16), these expressions further reduce to the following:

$$H_b = \dot{f}(t - \tau)u(t - \tau) \tag{19}$$

$$T_b = \dot{f}(t - \tau)\dot{u}(t - \tau) + \ddot{f}(t - \tau)u(t - \tau) \tag{20}$$

The fundamental relationships, given by Eqs. (19) and (20), can be used to compute the TES disturbance momentum and torque using the time derivatives of the function $f(t - \tau)$.

To determine the functional form of $f(t - \tau)$, a time-dependent analytical relationship for the thermal gradient at umbra entrance is assumed. Only sunset is considered due to the symmetry of the TES disturbance shown in Fig. 1. A relatively simple exponential function has been chosen and is expressed as

$$\begin{aligned} \Delta T_{\text{sunset}} &= q \qquad \text{if} \quad t < \tau_{\text{sunset}} \\ &= ce^{[-(t - \tau_{\text{sunset}})/p]} + b \qquad \text{if} \quad \tau_{\text{sunset}} \leq t < \tau_{\text{sunrise}} \end{aligned} \tag{21}$$

Substituting Eqs. (1) and (21) into Eq. (11) yields the following expression for I_b at sunset:

$$\begin{aligned} I_{b_{\text{sunset}}} \approx {} & \sum_{i=1}^{n} \left\{ \frac{l_i m_i d}{\alpha_{\text{cte}} q} \left[1 - \cos\left(\frac{l_i \alpha_{\text{cte}} q}{d}\right)\right] \right\} \\ & + \sum_{i=1}^{n} \left\{ \frac{l_i m_i d}{\alpha_{\text{cte}} \{ce^{[-(t - \tau_{\text{sunset}})/p]} + b\}} \right. \\ & \left. \times \left[1 - \cos\left(\frac{l_i \alpha_{\text{cte}} \{ce^{[-(t - \tau_{\text{sunset}})/p]} + b\}}{d}\right)\right] \right\} \end{aligned} \tag{22}$$

It can be seen that Eq. (22) is equivalent to Eq. (12) with

$$a_{\text{sunset}} = \sum_{i=1}^{n} \left\{ \frac{l_i m_i d}{\alpha_{\text{cte}} q} \left[1 - \cos\left(\frac{l_i \alpha_{\text{cte}} q}{d}\right)\right] \right\} \tag{23}$$

$$\begin{aligned} f(t - \tau_{\text{sunset}}) = {} & \sum_{i=1}^{n} \left\{ \frac{l_i m_i d}{\alpha_{\text{cte}} \{ce^{[-(t - \tau_{\text{sunset}})/p]} + b\}} \right. \\ & \left. \times \left[1 - \cos\left(\frac{l_i \alpha_{\text{cte}} \{ce^{[-(t - \tau_{\text{sunset}})/p]} + b\}}{d}\right)\right] \right\} \end{aligned} \tag{24}$$

If all subscripts are removed from Eq. (24) and, furthermore, if the thermal gradient is expressed as ΔT, then a general relation for the function $f(t-\tau)$ can be formulated as

$$f(t-\tau)=\sum_{i=1}^{n}\left\{\frac{l_i m_i d}{\alpha_{\text{cte}}\Delta T}\left[1-\cos\left(\frac{l_i\alpha_{\text{cte}}\Delta T}{d}\right)\right]\right\} \tag{25}$$

It is evident that Eq. (25) is equivalent to Eq. (11) after substitution of Eq. (1). This result makes sense as the physical relationships used to derive Eq. (11) must be contained in the mathematics. Thus, the momentum and torque equations can be computed using Eqs. (19) and (20), along with Eq. (25). They are as follows:

$$\begin{aligned} H_b &= 0 && \text{if} \quad t<\tau \\ &= \sum_{i=1}^{n} -\frac{l_i m_i d\Delta\dot{T}}{\alpha_{\text{cte}}\Delta T^2}\left[1-\cos\left(\frac{l_i\alpha_{\text{cte}}\Delta T}{d}\right)\right. \\ &\quad \left. -\frac{l_i\alpha_{\text{cte}}\Delta T}{d}\sin\left(\frac{l_i\alpha_{\text{cte}}\Delta T}{d}\right)\right] && \text{if} \quad t\geq\tau \end{aligned} \tag{26}$$

$$\begin{aligned} T_b &= 0 && \text{if} \quad t<\tau \\ &= T_\zeta+\frac{\Delta\ddot{T}H_b}{\Delta\dot{T}}-\frac{2\Delta\dot{T}H_b}{\Delta T} \\ &\quad +\sum_{i=1}^{n}\frac{l_i^3 m_i\alpha_{\text{cte}}\Delta\dot{T}^2}{d\Delta T}\cos\left(\frac{l_i\alpha_{\text{cte}}\Delta T}{d}\right) && \text{if} \quad t\geq\tau \end{aligned} \tag{27}$$

with

$$\begin{aligned} T_\zeta &= H_b && \text{if} \quad t=\tau \\ &= 0 && \text{if} \quad t>\tau \end{aligned} \tag{28}$$

where $\Delta\dot{T}$ and $\Delta\ddot{T}$ are the first and second time derivatives of the thermal gradient. The TES disturbance torque, described by Eqs. (27) and (28), possesses the two-part characteristic exhibited by the controlled response of the LANDSAT-4 satellite.

The TES disturbance model given by Eqs. (26–28) was developed under the assumption that ϕ_i remain <10 deg (0.176 rad). By replacing the trigonometric terms present in Eqs. (26–28) with the appropriate infinite series expansions and neglecting all second- and higher-order terms of ϕ_i, the TES disturbance equations can be reduced to

$$\begin{aligned} T_b &= 0 && \text{if} \quad t<\tau \\ &= T_\zeta+\sum_{i=1}^{n}\left(\frac{l_i^3 m_i\alpha_{\text{cte}}\Delta\ddot{T}}{2d}-\frac{l_i^5 m_i\alpha_{\text{cte}}^3\Delta\dot{T}^2\Delta T}{4d^3}\right)+\Theta(2) \\ & && \text{if} \quad t\geq\tau \end{aligned} \tag{29}$$

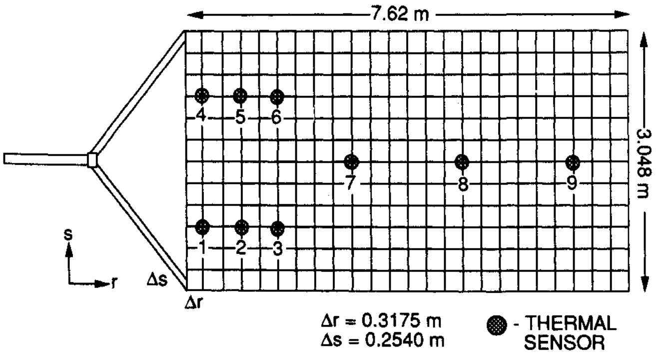

Fig. 3 Grid point locations superposed on the nine-element distributed thermal sensor network.

$$\begin{aligned} T_\zeta &= \sum_{i=1}^{n}\frac{l_i^3 m_i\alpha_{\text{cte}}\Delta\dot{T}}{2d}+\Theta(2) && \text{if} \quad t=\tau \\ &= 0 && \text{if} \quad t>\tau \end{aligned} \tag{30}$$

and

$$\begin{aligned} H_b &= 0 && \text{if} \quad t<\tau \\ &= \sum_{i=1}^{n}\frac{l_i^3 m_i\alpha_{\text{cte}}\Delta\dot{T}}{2d}+\Theta(2) && \text{if} \quad t\geq\tau \end{aligned} \tag{31}$$

where $[(l_i\alpha_{\text{cte}}\Delta T)/d]$ has been substituted for ϕ_i. The magnitude of ϕ_i is driven by the selection of the material properties, which in turn determine α_{cte} and influence the thermal gradient. The length, mass, and thickness of the appendage are generally dimensions that would not drive the value of ϕ_i too large. For example, consider an aluminum solar array with the following properties:

$$L = 7.62 \text{ m}$$

$$M = 215.0 \text{ kg}$$

$$d = 0.0315 \text{ m}$$

$$\alpha_{\text{cte}} = 23.4\times10^{-6}\ {}^\circ\text{C}^{-1}$$

If n is selected to be 25, then the maximum value of l_i ($i = 25$) using Eq. (5) is 7.4676 m. The corresponding value of ϕ_i for this example is 0.0759 assuming a thermal gradient of 15°C. This value is less than the limiting value of 0.176 and produces a value for ϕ_i^2 of 0.0056. The ratio of this neglected term with respect to the maximum value of 0.176 is approximately 0.03, or 3% of the limiting value. Thus, the simplified TES disturbance model would be valid for this example.

It is apparent from the preceeding discussion that the TES disturbance torque is not only a function of the thermal gradient across the array, but also is dependent on the first and second time derivatives of the thermal gradient. Thus, in order to predict the magnitude of the TES disturbance using the mathematical model, an accurate array temperature gradient profile is necessary.

Optimal Temperature Estimation

The dependence of the TES disturbance torque model on the successive derivatives of the thermal gradient motivates the need for accurate temperature determination. To estimate the TES disturbance, the thermal response of a solar array may be predicted using numerical techniques. Such methods include using the TRASYS[8] and SINDA[9] software packages as well as solving the one-dimensional heat equation using finite difference approximations.[6,10] However, to evaluate the true nature of the TES disturbance, thermal sensors can be used to measure the actual thermal response of the structure during on-orbit spacecraft operation. Two types of thermal sensors, thermistors and platinum resistance thermometers (PRTs), are presently utilized for spaceflight applications. Fully integrated (i.e., signal conditioned) thermistors are accurate to about ± 4°C, whereas the accuracy of a fully integrated PRT is approximately ± 1°C.[11] Spacecraft thermal sensor hardware simply consists of two resistors in parallel, one exposed to the environment and the other shielded from the outside, supplied with a constant current source. The measured voltage across the resistor is an indication of the temperature. The function of the additional resistor is to linearize the nonlinear relationship between temperature and resistance over the thermal sensor operating range.

If a distributed network of thermal sensors exists on each surface of an array, as illustrated in Fig. 3 for the front surface, a measurement of the surface temperatures at those prescribed locations is obtained. However, all of the thermal sensors may not be operating at the same time (e.g., some may be used for redundancy) and, futhermore, the sensors may not be positioned at optimally selected locations. Yet it would be advantageous to use all of the available surface temperature information to estimate the array surface temperature at a consistent desired location. Thus, a technique based on the Gauss-Markov theorem is described to optimally estimate array surface temperatures. Once a temperature estimate for each surface is determined, the thermal gradient may be predicted by differencing the front and back surface temperatures at the specified location. This approach differs from the numerical methods in that the thermal gradient is computed using temperature measurements from each surface without consideration of the internal composition of the array. First-order differencing techniques can then be employed to calculate the first and second time derivatives of the thermal gradient.

The Gauss-Markov theorem provides a linear minimum mean square estimate of a vector $\boldsymbol{x}$ with n_1 components given a set of n_2 observations $\boldsymbol{\Theta}$. The estimator, given by Liebelt,[12] is stated as follows:

$$\hat{\boldsymbol{x}} = C_{x\Theta}C_{\Theta}^{-1}\boldsymbol{\Theta} \tag{32}$$

where the error matrix associated with the estimate of $\boldsymbol{x}$ is given as

$$C_e = C_x - C_{x\Theta}C_{\Theta}^{-1}C_{x\Theta}^T \tag{33}$$

If the expected value of the estimate $E(\hat{\boldsymbol{x}})$ is equal to $\boldsymbol{x}$ (i.e., the average of the estimate is equal to the true value), then $\hat{\boldsymbol{x}}$ is a linear minimum variance unbiased estimate and C_e is the covariance matrix of the estimate.

Equations (32) and (33) form the basis of the optimal estimation method developed by Bretherton et al.[13] For their analysis, the Gauss-Markov theorem was utilized to estimate the value of a two-dimensional scalar variable at a specified location given measurement data at a limited number of positions. A linear form of the observations is assumed and can be expressed, for $j = 1, \ldots, N$, as

$$\varphi_j = \Theta(r,s) + \epsilon_j \tag{34}$$

Furthermore, the assumption is made that the measurement errors are uncorrelated and independent of φ. Under these assumptions, Bretherton et al.[13] applied the Gauss-Markov theorem, Eqs. (32) and (33), to obtain the resulting estimation equation

$$\hat{\Theta} = \bar{\Theta} + \sum_{j=1}^{N} C_{xj}\left[\sum_{k=1}^{N} A_{jk}^{-1}(\varphi_k - \bar{\Theta})\right] \tag{35}$$

and the associated error matrix C_e given as

$$C_e = C_x - \sum_{j=1}^{N}\sum_{k=1}^{N} C_{xj}C_{xk}A_{jk}^{-1} \tag{36}$$

The estimated mean of the observations is computed such that the sum of the weighted measurements equals zero and is given as[13]

$$\bar{\Theta} = \frac{\sum_{j=1}^{N}\sum_{k=1}^{N} A_{jk}^{-1}\varphi_k}{\sum_{j=1}^{N}\sum_{k=1}^{N} A_{jk}^{-1}} \tag{37}$$

Equations (35-37) are thus used to provide an optimal estimate of a solar array temperature at a prescribed location and its associated error.

Application

The key to implementing the optimal estimation technique is the determination of both the C_x matrix and an analytic weighting function to scale the variance of the data. The weighting function is necessary to compute numerical values for the C_{xj} and A_{jk} matrices. The C_x matrix is generally unknown but can be approximated by the variance of the given data set. The numerical computation of C_x is generated using the following equation[13]:

$$C_x = \sigma_\varphi^2 + \frac{\left(1 - \sum_{j=1}^{N}\sum_{k=1}^{N} C_{xj}A_{jk}^{-1}\right)^2}{\sum_{j=1}^{N}\sum_{k=1}^{N} A_{jk}^{-1}} \tag{38}$$

where σ_φ is the standard deviation of the measurement data given as

$$\sigma_\varphi = \sqrt{\frac{\sum_{j=1}^{N}(\varphi_j - \bar{\varphi})^2}{N-1}} \tag{39}$$

with

$$\bar{\varphi} = \frac{\sum_{j=1}^{N}\varphi_j}{N} \tag{40}$$

The last term on the right side of Eq. (38) accounts for uncertainties associated with the estimated mean.

A weighting function is selected for this research to scale the measurements according to their spatial location with respect to one another and to the specified position of the estimate. It is desired that the significance of a measurement decrease exponentially with distance from either the position of the estimate or another measurement over a region of influence. This type of weighting function can be used as a first cut statistical model given no a priori knowledge of the data statistics. The estimation technique can, however, easily accommodate more complex statistical models if desired. An analytical expression for the weighting function is given as

$$W_{jk} = 0.2(\gamma - \bar{r}_{jk}^2 - \bar{s}_{jk}^2)\exp\left[-\sqrt{\bar{r}_{jk}^2 + \bar{s}_{jk}^2}\right] \tag{41}$$

The parameter γ is introduced to change the quality of the observations. If γ is set equal to 5.0, then a maximum weight of 1.0 will exist when the condition $j = k$ is satisfied in Eq. (41). As γ linearly decreases, the maximum attainable weight also decreases in a linear fashion. The scaling parameters $\bar{r}_{jk}$ and $\bar{s}_{jk}$ are calculated using the following equations:

$$\bar{r}_{jk} = \frac{r_j - r_k}{r_{\text{scale}}} \tag{42}$$

$$\bar{s}_{jk} = \frac{s_j - s_k}{s_{\text{scale}}} \tag{43}$$

The variables r_{scale} and s_{scale} can be specified to determine an effective range of data influence (decorrelation scale) or set to the dimensions of the spatial area over which the measurements are confined. For the present study, the latter condition is assumed. The variables r_j and s_j denote the spatial location of the jth observation, whereas the variables r_k and s_k indicate the spatial position of the kth data point. Thus, given the weighting function, a spatially weighted covariance can be computed between the point of estimation and the measurements C_{xj} and between the observations themselves A_{jk}. The calculation of C_{xj} can be expressed by

$$C_{xj} = W_{xj}\sigma_\varphi^2 \tag{44}$$

where the subscript x is used to denote the desired location (r_x, s_x) of the estimate; the weighted observation matrix A_{jk} is determined from the following equation:

$$A_{jk} = W_{jk}\sigma_\varphi^2 + \sigma_\epsilon^2\delta_{jk} \tag{45}$$

where δ_{jk} is the Kronecker delta function expressed as

$$\begin{aligned} \delta_{jk} &= 0 \qquad \text{if} \qquad j \neq k \\ &= 1 \qquad \text{if} \qquad j = k \end{aligned} \tag{46}$$

and σ_ϵ is the standard deviation of the measurement error.

The one drawback of using this technique is the inversion of the observation covariance matrix A_{jk}, which has dimensions equal to the number of observations N. If a large number of observations exist then the dimension of the covariance matrix becomes large and hard to numerically invert. However, to speed the numerical inversion process, the order of the covariance matrix can be reduced by keeping only those observations having a weight value above a specified limit.

Results

Assume that the solar array has physical dimensions of 7.62 × 3.048 × 0.0315 m and, furthermore, that the length and width of the array represent the spatial area scales r_{scale} and s_{scale}, respectively. The arrangement of the thermal sensors on a typical solar array surface, labeled 1-9 in Fig. 3, represent the spatial locations of each temperature observation. Since the optimal temperature estimation technique has the ability to provide a temperature estimate at any location, a grid of temperature estimates can be generated to characterize the temperature profile of the entire array using a finite set of data observations. The grid point locations are illustrated in Fig. 3 where the incremental distances between nodes are $\Delta r = 0.3175$ m and $\Delta s = 0.2540$ m. To assess the accuracy of the estimation technique, grid points were collocated with the thermal sensor positions, as shown in Fig. 3.

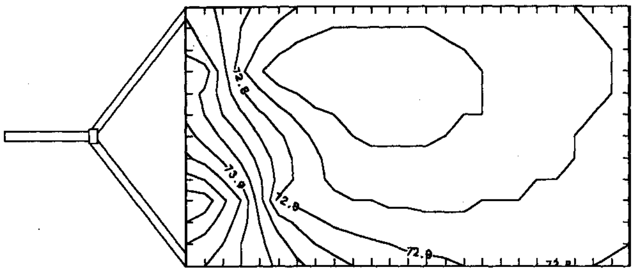

CONTOUR INTERVAL 0.05°C

CONTOUR FROM 72.65°C TO 73.15°C

Fig. 4 Temperature estimates for array front surface (case 2).

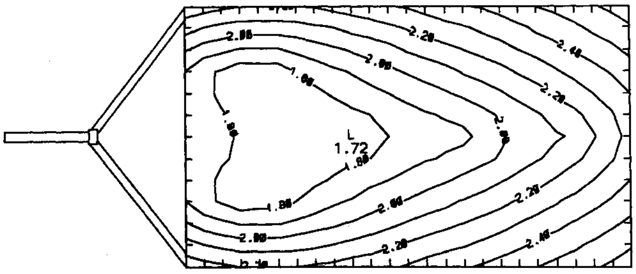

CONTOUR INTERVAL 0.1°C

CONTOUR FROM 1.70°C TO 2.60°C

Fig. 5 Temperature standard deviations for array front surface (case 2).

To demonstrate the technique, temperature measurements at each of the nine thermal sensor locations, all at a single point in time, were generated using a simple thermal model.[6] These estimates are assumed perfect, e.g., $\epsilon_j = 0$, and are provided in Table 1 under the case 1 heading along with the nine sensor positions. Also listed in Table 1 are two additional sets of simulated temperature measurements. The case 2 data represent thermistor observations, where the true temperature data have been corrupted by a uniformly distributed random variable with zero mean and a standard deviation of 4°C. In a similar fashion, PRT sensor measurments, listed under the case 3 heading, were created using a uniformly distributed random variable also with zero mean, but a 1°C standard deviation. Because of the uniformity of the true data (i.e., approximately 0.1°C separation between the maximum and minimum temperatures), the optimal estimation technique will first be demonstrated using the simulated thermistor data (case 2).

Utilizing Eqs. (35-45), a temperature estimate at each grid point is computed, where the factor γ is set equal to 5.0 to provide a maximum weight of 1.0. The contoured array front surface temperature profile is shown in Fig. 4. Notice how the contour changes rapidly over the two regions associated with the lowest temperature measurements (e.g., sensors 3, 5, and 6). Overall, however, the large deviations in sensor temperatures are smoothed giving an estimated temperature range of about 72.5-73.2°C. The standard deviations associated with the array front surface temperature estimates are presented in Fig. 5. From Fig. 5, it is clear that the smallest standard deviations are associated with the thermal sensor positions. In the areas where observations are limited, the standard deviation increases. The contoured back panel is presented in Fig. 6 with the temperature standard deviations given in Fig. 7. The highs and lows shown in Fig. 6 are a direct result of the thermal sensor observations. In a physical sense, these regions would be attributed to hot and cold spots on the array. Again, Fig. 7 illustrates the correlation between temperature uncertainty and the thermal sensor locations. A thermal gradient estimate, across the array thickness, is computed by subtracting the two surface temperature estimates at each grid point and is shown in Fig. 8. The structure of the contoured

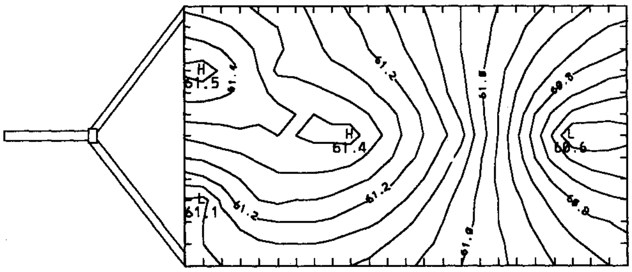

CONTOUR INTERVAL 0.05°C

CONTOUR FROM 60.60°C TO 61.45°C

Fig. 6 Temperature estimates for array back surface (case 2).

Table 1 Thermal sensor locations and temperature measurements for cases 1-3

Sensor number	Sensor position		Temperature, °C					
			Case 1 (true)		Case 2 (thermistor)		Case 3 (PRT)	
	r, m	s, m	Front	Back	Front	Back	Front	Back
1	0.3175	0.762	72.8795	60.5102	75.6214	57.8954	73.8198	59.8565
2	0.9525	0.762	72.9475	60.6052	75.1302	63.2903	72.4815	61.2765
3	1.5875	0.762	72.9530	60.6156	69.0273	61.5998	73.5481	60.8616
4	0.3175	2.286	72.8510	60.5141	76.0959	63.7727	73.4943	61.3288
5	0.9525	2.286	72.9433	60.6072	70.5750	61.6657	72.3178	60.8719
6	1.5875	2.286	72.9525	60.6153	71.1157	59.6889	73.8453	60.3837
7	2.8575	1.524	72.9534	60.6162	72.4241	63.0318	72.9780	61.2201
8	4.7625	1.524	72.9534	60.6162	72.7547	62.6133	72.4672	61.1155
9	6.6675	1.524	72.9534	60.6162	72.8162	57.2821	72.7367	59.7826

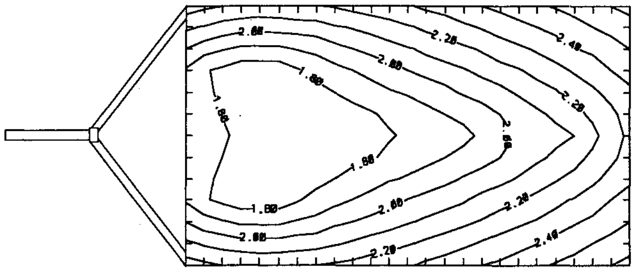

CONTOUR INTERVAL 0.1°C

CONTOUR FROM 1.70°C TO 2.60°C

Fig. 7 Temperature standard deviations for array back surface (case 2).

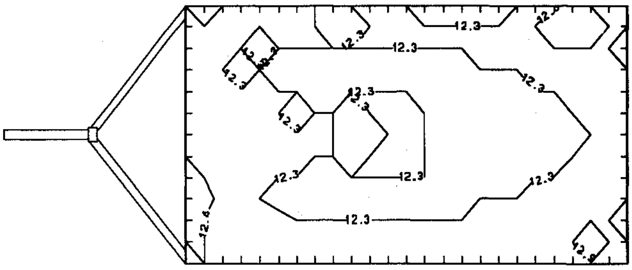

CONTOUR INTERVAL 0.02°C

CONTOUR FROM 12.32°C TO 12.36°C

Fig. 10 Thermal gradient estimates for array (case 1).

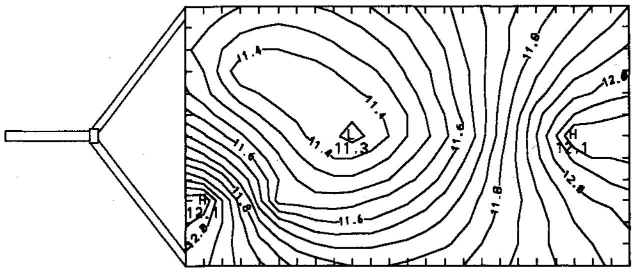

CONTOUR INTERVAL 0.05°C

CONTOUR FROM 11.30°C TO 12.10°C

Fig. 8 Thermal gradient estimates for array (case 2).

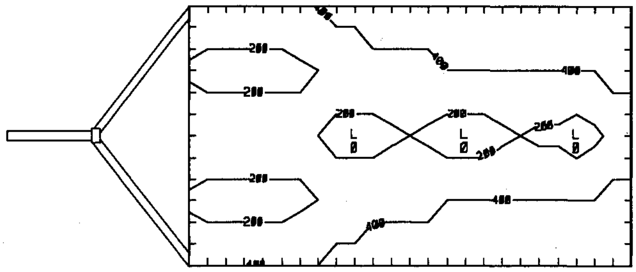

CONTOUR INTERVAL 0.02°C

CONTOUR FROM 0.00°C TO 0.04°C

CONTOURS SCALED BY 10000

Fig. 11 Thermal gradient standard deviations for array (case 1).

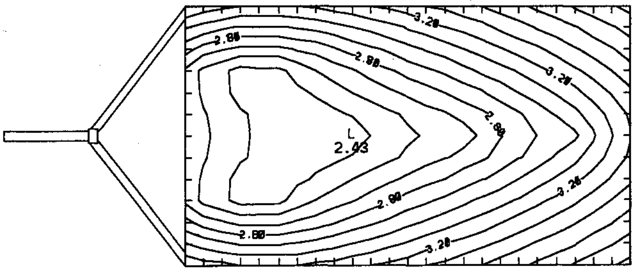

CONTOUR INTERVAL 0.1°C

CONTOUR FROM 2.40°C TO 3.70°C

Fig. 9 Thermal gradient standard deviations for array (case 2).

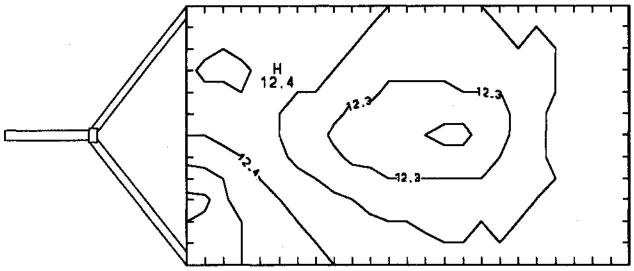

CONTOUR INTERVAL 0.04°C

CONTOUR FROM 12.20°C TO 12.44°C

Fig. 12 Thermal gradient estimates for array (case 3).

thermal gradient mimics the back surface temperature contours since the front surface is reasonably consistent. The standard deviation of the thermal gradient estimates, given in Fig. 9, is obtained by performing a root sum squared (RSS) on the front and back surface standard deviations.

Employing the same methodology, the estimated thermal gradients and standard deviations for cases 1 and 3 are constructed and illustrated in Figs. 10 and 11 for the true data and Figs. 12 and 13 for the simulated PRT measurements. The case 1 thermal gradient, Fig. 10, is essentially constant with a value of 12.3°C at all grid points. The error covariance of the unbiased estimates is zero at each thermal sensor position and minimal in all other regions. The PRT (case 3) thermal gradient estimates, Fig. 12, reflect highs and lows present in the two surface estimates, but remain fairly uniform ranging from 12.2 to 12.4°C. Figure 13 again shows the relationship between the minimum uncertainty in the estimated temperature gradient field and the thermal sensor locations. Comparison of the three cases shows that the largest standard deviations are associated with the thermistor data (case 2) and are a result of the large variance associated with the simulated thermistor data set.

Table 2 depicts the exact and estimated temperature gradients at each of the nine thermal sensor locations along with the percent difference between them. The exact data is computed by directly differencing the front and back sensor observations. A comparison using the percent difference between the exact and estimated true data shows excellent agreement with the largest deviation being only 0.08%. The maximum difference deviation for the thermistor data is 8.18%, whereas the largest percent difference for the PRT estimates is 0.89%. From Table 2, it is evident that the difference for all three cases is < 10%, with the estimated true and PRT data remaining below 1%. The uncertainty associated with each temperature gradient estimate is also small, indicating a small dispersion from the true gradient, thus providing a reasonable estimate for these three cases.

If the parameter γ is allowed to approach 0 from its maximum value of 5.0, the assumed quality of the observations is degraded. Furthermore, as γ decreases the estimate is expected to degrade with an increase in the standard deviation. To test this hypothesis, front surface temperature estimates and standard deviations for the three test cases were recomputed, at a single spatial location, for values of γ ranging from 0.1 to 5.0 in 0.1 increments. The prescribed point of estimation is arbitrarily selected to be (3.810, 0.508) m. Figures 14 and 15 show the estimated temperatures and standard deviations, respectively, for the true data (case 1), the thermistor data (case 2),

Table 2 Comparison of simulated thermal sensor data to simulated array thermal gradient estimates

Sensor number	Temperature, °C Exact	Temperature, °C Estimated true	% Error	Temperature, °C Estimated thermistor	% Error	Temperature, °C Estimated PRT	% Error
1	12.37	12.37	0.00	12.10	2.18	12.45	0.65
2	12.34	12.34	0.00	11.82	4.21	12.37	0.24
3	12.34	12.33	0.08	11.53	6.56	12.36	0.16
4	12.34	12.34	0.00	11.50	6.81	12.31	0.24
5	12.34	12.33	0.08	11.36	7.94	12.31	0.24
6	12.34	12.33	0.08	11.37	7.86	12.35	0.08
7	12.34	12.33	0.08	11.33	8.18	12.26	0.65
8	12.34	12.33	0.08	11.59	6.08	12.23	0.89
9	12.34	12.33	0.08	12.15	1.54	12.35	0.08

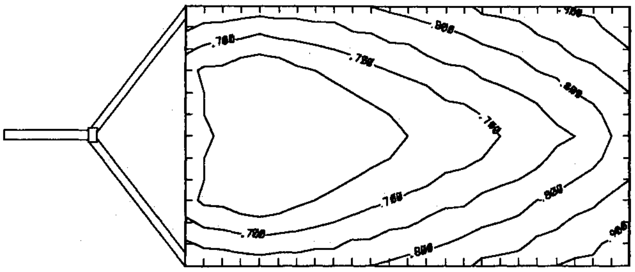

CONTOUR INTERVAL 0.05°C

CONTOUR FROM 0.60°C TO 0.90°C

Fig. 13 Thermal gradient standard deviations for array (case 3).

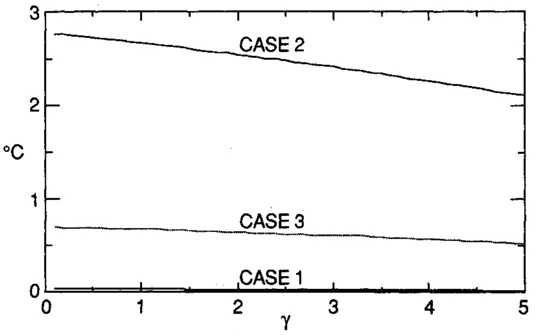

Fig. 15 Temperature standard deviations for cases 1, 2, and 3 vs γ.

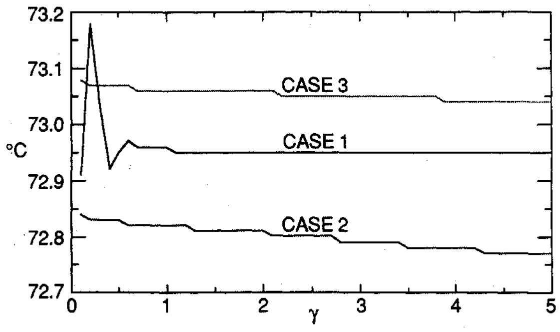

Fig. 14 Temperature estimates for cases 1, 2, and 3 vs γ.

and the PRT data (case 3). An inspection of Fig. 14 reveals that the temperature estimate for case 1 remains essentially constant, 72.95°C, for $\gamma \geq 1.0$. In the range of $\gamma < 1.0$, the case 1 temperature estimate reaches a maximum of 73.18°C at $\gamma = 0.2$ and a minimum of 72.92°C at $\gamma = 0.4$. The large deviations occur as the elements of the A_{ij} matrix approach small values, resulting in an inverse matrix with large components. Both cases 2 and 3 exhibit a linear change in the temperature estimate over the entire range of γ. The case 2 thermistor estimate begins with a temperature value of 72.84°C at $\gamma = 0.1$ and continues with a decreasing slope of $0.014°\text{C}/\gamma_{\text{increment}}$ to reach a final temperature of 72.77°C when $\gamma = 5.0$. The case 3 temperature estimate decreases with a slope of approximately $0.008°\text{C}/\gamma_{\text{increment}}$ with a temperature of 73.04°C at $\gamma = 5.0$. The standard deviations for the three cases, as a function of γ, are illustrated in Fig. 15. The standard deviation for the ideal sensor (case 1) ranges from 0.04°C at $\gamma = 0.1$ to 0.02°C at $\gamma = 5.0$ with a linear characteristic. The simulated thermistor data set (case 2) shows the sharpest linear decrease in standard deviation from 2.76 to 2.11°C with a slope of $-0.13°\text{C}/\gamma_{\text{increment}}$. Uncertainty in the simulated PRT data also shows a linearly decreasing trend but with a much more subtle slope of $0.03°\text{C}/\gamma_{\text{increment}}$. As expected, the estimates for the three cases degrade with an associated increase in the standard deviation as γ approaches a small value. Furthermore, except for the case 1 temperatures for small γ ($\gamma < 0.3$), estimates for each of the three cases fall within the range of the observed data with case 2 exhibiting the largest standard deviation.

Conclusions

An optimal temperature estimation technique has been described and used to estimate the surface temperatures of a satellite solar array at a set of prescribed locations given data from a distributed thermal sensor network at a single point in time. The technique also provides error information relative to the estimated variable. This technique is capable of determining array surface temperatures at any location, with reasonable accuracy, from a finite set of observational data. Applying the procedure to both surfaces of the array, as a function of time, and differencing the surface temperature estimates will result in an estimated thermal gradient profile. The thermal gradient estimates can then be utilized to drive the TES disturbance model in order to evaluate the true nature of the TES disturbance.

References

[1] Sudey, J., and Schulman, J. R., "In-Orbit Measurements of LANDSAT-4 Thematic Mapper Dynamic Disturbances," *Acta Astronautica,* Vol. 12, No. 7/8, 1985, pp. 485–503.

[2] Jasper, P. E., and Neste, S., "UARS Solar Array Snap," General Electric Space Division, U-1K21-UARS-481, Philadelphia, PA, July 1986.

[3] Vigneron, F. R., and Millar, R. A., "Flight Performance of the Stabilization System of the Communications Technology Satellite," *Journal of Guidance and Control,* Vol. 1, No. 6, 1978, pp. 404–412.

[4] Nurre, G. S., Sharkey, J. P., and Waites, H. B., "Initial Performance Improvements due to Design Modifications for the Pointing Control System on the Hubble Space Telescope," American Astronomical Society, Washington, DC, Paper 91-071, Feb. 1991.

[5] Dennehy, C. J., Kia, T., and Welch, R. V., "Attitude Determination and Control Subsystem for the TOPEX Satellite," AIAA Paper 88-4129, Aug. 1988.

[6] Zimbelman, D. F., "Thermal Elastic Shock and Its Effect on TOPEX Spacecraft Attitude Control," American Astronomical Society, Washington, DC, Paper 91-056, Feb. 1991.

[7] Kaplan, W., *Operational Methods for Linear Systems,* Addison-

Wesley, Reading, MA, 1966, pp. 49–51.

[8] Jensen, C. J., and Goble, R. G., "Thermal Radiation Analysis SYStem (TRASYS) User's Manual," Martin Marietta Astronautics Group, Denver, CO, NAS9-15832, Oct. 1986.

[9] Smith, J. P., "SINDA Users' Manual," TRW Systems Group, Redondo Beach, CA, NAS9-10435, April 1971.

[10] Bainum, P. M., Hamsath, N., and Krishna, R., "The Dynamics and Control of Large Space Structures After the Onset of Thermal Shock," *Acta Astronautica,* Vol. 19, No. 1, 1989, pp. 1–8.

[11] Zimbelman, D. F., "Thermal Elastic Shock and Its Effect on Spacecraft Attitude Control," Ph.D. Dissertation, University of Colorado, Boulder, CO, Aug. 1990.

[12] Liebelt, P. B., *An Introduction to Optimal Estimation,* Addison-Wesley, Reading, MA, 1967, pp. 135–151.

[13] Bretherton, F. P., Davis, R. E., and Fandry, C. B., "A Technique for Objective Analysis and Design of Oceanographic Experiments Applied to MODE-73," *Deep Sea Research,* Vol. 23, 1976, pp. 559–582.

Earl A. Thornton
Associate Editor

Attention Journal Authors: Send Us Your Manuscript Disk

AIAA now has equipment that can convert **virtually any disk** (3½-, 5¼-, or 8-inch) **directly to type**, thus avoiding rekeyboarding and subsequent introduction of errors.

The following are examples of easily converted software programs:

- PC or Macintosh T^{E}X and LAT^{E}X
- PC or Macintosh Microsoft Word
- PC Wordstar Professional

You can help us in the following way. If your manuscript was prepared with a word-processing program, please *retain the disk* until the review process has been completed and final revisions have been incorporated in your paper. Then send the Associate Editor *all* of the following:

- Your final version of double-spaced hard copy.
- Original artwork.
- A *copy* of the revised disk (with software identified).

Retain the original disk.

If your revised paper is accepted for publication, the Associate Editor will send the entire package just described to the AIAA Editorial Department for copy editing and typesetting.

Please note that your paper may be typeset in the traditional manner if problems arise during the conversion. A problem may be caused, for instance, by using a "program within a program" (e.g., special mathematical enhancements to word-processing programs). That potential problem may be avoided if you specifically identify the enhancement and the word-processing program.

In any case you will, as always, receive galley proofs before publication. They will reflect all copy and style changes made by the Editorial Department.

We will send you an AIAA tie or scarf (your choice) as a "thank you" for cooperating in our disk conversion program. Just send us a note when you return your galley proofs to let us know which you prefer.

If you have any questions or need further information on disk conversion, please telephone Richard Gaskin, AIAA Production Manager, at (202) 646-7496.

AIAA